Nanoscale Advances

ROYAL SOCIETY OF CHEMISTRY

PAPER

View Article Online
View Journal | View Issue

Cite this: *Nanoscale Adv.*, 2021, **3**, 4597

Metal nanoparticles entrapped in metal matrices†

Dina Pinsky,[a] Noam Ralbag,[a] Ramesh Kumar Singh,[bc] Meirav Mann-Lahav,[b] Gennady E. Shter,[b] Dario R. Dekel,*[bc] Gideon S. Grader*[bc] and David Avnir*[a]

We developed synthetic methods for the doping of metals (M) with metallic nanoparticles (NPs). To the best of our knowledge – unlike oxides, polymers and carbon-based supports – metals were not used so far as supporting matrices for metallic NPs. The composites (denoted M1-NPs@M2) comprise two separate phases: the metallic NPs (the dopant) and the entrapping 3D porous metallic matrix, within which the NPs are intimately held and well dispersed. Two different general synthetic strategies were developed, each resulting in a group of materials with characteristic structure and properties. The first strategy uses pre-prepared NPs and these are entrapped during reductive formation of the metallic matrix from its cation. The second strategy is *in situ* growth of the doped metallic NPs within the pre-prepared entrapping metallic matrix. These two methods were developed for two types of entrapping metallic matrices with different morphologies: porous aggregated metallic matrices and metallic foams. The leading case in this study was the use of Pt as the NP dopant and Ag as the entrapping matrix, using all of the four combinations – entrapment or growth within aggregated Ag or Ag foam matrices. Full physical and chemical properties analysis of these novel types of materials was carried out, using a wide variety of analytical methods. The generality of the methods developed for these bi-metallic composites was investigated and demonstrated on additional metallic pairs: Au NPs within Ag matrices, Pd NPs within Ni matrices and Ir-NPs within a Rh matrix. As the main application of metallic NPs is in catalysis, the catalytic activity of M1-NPs@M2 is demonstrated successfully for entrapped Pt within Ag for reductive catalytic reactions, and for Pd within Ni for the electrocatalytic hydrogen oxidation reaction.

Received 28th April 2021
Accepted 9th July 2021

DOI: 10.1039/d1na00315a

rsc.li/nanoscale-advances

1. Introduction

Metallic nanoparticles (NPs) have entered practically every modern facet of the natural sciences, including catalysis, optics, sensing, biomedicine, and more. Many of these applications require the dispersion of the NPs in or on solid supports, in order to avoid their aggregation, to ease their transport and after-use separation, to allow their use as components in devices, and to stabilize them against environmental deterioration. The solid-materials world, offers three large families of supports for metallic NPs: (I) ceramics and glasses (such as silica, alumina, zirconia, titania, *etc.*, in the forms of sol–gel matrices, aerogels, zeolites and more[1]); (II) carbon-based materials (polymers, plastics, MOFs, biopolymers, various forms of carbon[2]); and, (III) metals. Of these three families, the first two have been used intensively as supports of metallic NPs, but not – and this comes as a surprise – the third large family of metals. The main focus of this report is to draw attention to the concept of using metals as supports of metallic NPs, and to offer synthetic routes for such immobilizations. Many of the physical and chemical properties of metals are unique to this family, which has properties not found in the plentitude of non-metallic supports that have been used so far: metals are excellent electric conductors; they are excellent heat conductors; they are malleable and ductile to desired shapes; many of the metals are biocompatible (Au, Pt) and chemically stable; endless alloy combinations allow fine tuning of desired properties; dual activity of metallic dopant and matrix become possible; and synergism between dopant and matrix may emerge (as shown in this report). All of these expand the arsenal of the materials in the design of catalytic, electrocatalytic, and sensing systems. It should be noted that bimetallic (or multi-metallic) materials can also form alloys in which one element penetrates into the crystal lattice of another[3] forming "solid solutions"; we refer, however, to a metallic composite in which the supporting matrices and the entrapped NP metals are well defined different phases. It is also of relevance to mention metal–metal core–shell materials, for instance, Au-core/Pd-shell NPs[4,5] and Pd-core/Pt-shell;[6] yet in this architecture, the exposed surface is of the shells only, unlike high surface area porous supports of NPs.

[a]*Institute of Chemistry and the Center for Nanoscience and Nanotechnology, The Hebrew University of Jerusalem, Jerusalem 9190401, Israel. E-mail: David.Avnir@mail.huji.ac.il*

[b]*The Wolfson Department of Chemical Engineering, Technion-Israel Institute of Technology, Haifa 3200003, Israel. E-mail: dario@technion.ac.il; grader@technion.ac.il*

[c]*The Nancy & Stephen Grand Technion Energy Program (GTEP), Technion –Israel Institute of Technology, Haifa 3200003, Israel*

† Electronic supplementary information (ESI) available. See DOI: 10.1039/d1na00315a

Of the two approaches we developed for obtaining metal-entrapped metals (denoted M1-NP@M2), the first one requires introductory background, as it uses a special materials methodology, namely that of molecularly doped metals.[7,8] This methodology allows the three-dimensional (3D) encaging of dopants in porous metallic matrices, that is, the molecule is surrounded all around it by metallic NPs in cages which keep it from being washed away, while allowing accessibility through the interstitial porosity of the aggregates. It is quite general and a wide variety of dopants – dyes, antibacterial agents and drugs, enzymes, polymers, chiral molecules, and catalytic complexes, have been entrapped in various metals, including Ag, Pt, Pd, Cu, Fe, Co, Au, and various alloys.[7,8] Recently, this methodology was extended to the entrapment of non-metallic NPs as dopants: ceria-NPs@Pd,[9] magnetic strontium hexaferrite-NPs@coin metals[10] and CdSe/CdS core-SiO_2 shell entrapped in thin films of Au.[11] The main methods for obtaining these dopant@M materials are based on the reduction of the metal cation of the entrapping metal in the presence of the dopant to be entrapped, and specific reduction processes include using homogeneous reducing agents, heterogeneous reducing agents, using the solvent for the reduction, electrochemical reduction and more.[8] As in the case of molecules, a NP-dopant is held tightly inside the cages of the aggregated porous matrix, but on the other hand, is accessible to react with external reagents. There are significant differences between this 3D entrapment process and 2D adsorption: the adsorbed dopant is exposed, while the 3D entrapment protects the molecule all around it; while in adsorption or covalent attachment, only one moiety of the molecule is in contact with the metal, in the 3D entrapment *all* parts of it touch the metal; and, while adsorbed molecules are easily washed, entrapped ones are difficult to extract.[12] Nevertheless, the accessibility of the dopant for the external environment opens applications such as catalysis and sensing. While the first method for obtaining M1-NP@M2 utilized pre-prepared M1-NPs and the reductive synthesis of M2, the second approach presented here does the opposite: it utilized pre-prepared porous matrix of M2, and synthesizes the M1-NPs using the M2 as a reducing agent – this is described in detail below.

The two methods for entrapping metallic NPs were developed for two types of metallic matrices with different morphologies: porous aggregated matrices, and metal-foam matrices. All and all, we have therefore four options for M1-NP@M2, each with its unique characteristics and properties, as detailed below. Pt as a dopant and Ag as an entrapping metallic matrix were chosen as a leading case of this report and are described in detail. The generality of the methods developed was investigated and demonstrated on several additional metallic pairs: Au-NPs within Ag matrices, Pd-NPs within Ni matrices and Ir-NPs within Rh matrix. As the main application of metallic NP has been their use as supported catalysts, we demonstrate the feasibility of the use of metals as supports of catalytic metallic NPs – we believe for the first time – on two catalytic processes: Pt-catalyzed reductive degradations of dyes with Pt-NPs entrapped in silver and the electrocatalytic hydrogen oxidation reaction (HOR) with Pd-NPs in Ni.

2. Experimental details

2.1 Chemicals, instrumentation and analytical methods

See ESI, Sections 1.1 and 1.2.†

2.2 Materials syntheses

Synthesis of the NPs. See ESI Section 1.3 for synthetic details and Fig. S1.† The average particles sizes of all NPs used in this study are summarized in Table 1, and were calculated by averaging the size of 100 particles in TEM images (Fig. S1, (including a typical histogram), ESI†).

Entrapment of Pt-NPs within porous Ag – type-A, denoted Pt@Ag. 6.0 mL of the prepared Pt-NPs suspension (0.032 mmol of Pt) was diluted to 10 mL with TDW, in a 25 mL vial. 314.9 mg of $AgNO_3$ (1.85 mmol) was added to the solution and stirred for a few minutes. 122 μL of H_3PO_2 (2.25 mmol) was added for the reduction of the Ag cations. The solution was stirred overnight, at the end of which the upper solution became transparent. The upper solution was decanted and then suspended in 10 mL of NH_4OH 25% w and stirred for 15 minutes, followed by two washing steps of 10 mL of TDW for 10 suspension minutes each. The powder was filtered with a nylon filtering paper and dried in a desiccator under vacuum overnight. The filtrate was tested with NaCl for remains of unreduced Ag ions. The composite was grinded and then weighted and kept in a vial. Here and below, the yield of the reductions is qualitative, with about 10% loss during the cleaning and filtering processes. For comparative purposes and for the *in situ* method (below), the pure porous silver was prepared by the same method but without the dopant except that the reduction time was changed to 8 hours. Here and below, purity was determined by thermogravimetric analysis (TGA) performed in air at a temperature range of 50–950 °C which revealed less than 1 wt% PVP, small quantities of water, and traces of AgCl.

Entrapment of Pt-NPs within Ag foam – type B, denoted Pt@Ag-foam. The formation of the silver foam follows ref. 13 with modifications: 6.0 mL of the prepared Pt-NPs suspension (0.032 mmol of Pt) was diluted to 25 mL of TDW in a 100 mL beaker. 314.9 mg of $AgNO_3$ (1.85 mmol) was added to the solution and stirred for a few minutes. 349.6 mg of $NaBH_4$ (9.24 mmol) was added for the reduction of Ag, which resulted in the immediate formation of bubbles and emission of gas. The composite was stirred for an hour, until the upper solution was transparent. The upper solution was decanted and then and suspended with 10 mL of NH_4OH 25% and stirred for 15 minutes, followed by two washing steps of 10 mL of TDW for 10 suspension minutes each. The powder was filtered with a nylon filtering paper and dried in a desiccator under vacuum overnight. The filtrate was tested with NaCl for remains of

Table 1 Nanoparticles average sizes

NPs element	Pt	Au	Ir	Pd
Size (nm)	1.7 ± 0.4	1.9 ± 0.7	1.7 ± 0.6	2.8 ± 0.8

unreduced Ag ions. The composite was grinded and mixed, weighed and kept in a vial. For comparative purposes, the pure foam silver was prepared by the same method, but without the dopant.

***In situ* generation of platinum in porous Ag – type C, denoted Pt-grown@Ag.** 200 mg of pure Ag (1.85 mmol) prepared by the procedure of type A, was added to 10 mL of TDW, in a 25 mL vial. 329.0 mg of PVP was added to the solution and stirred for 30 minutes. Afterwards, 62 μL of H_2PtCl_6 solution 0.5 M (0.031 mmol) was added and the composite was stirred for approximately an hour. The upper solution changed its color from yellow to colorless, while the Ag powder was covered with a darker Pt layer. The composite was then washed with 10 mL of NH_4OH for 15 minutes, followed by two washing steps of 10 mL of TDW for 10 suspension minutes each. Afterward, the powder was filtered, dried and grinded.

***In situ* generation of platinum in silver foam-type D, denoted Pt-grown@Ag-foam.** The composite was prepared similarly to type C, using the pure Ag foam (described in type B).

Syntheses of all other M1-NP@M2 composites. For the entrapment of Au within Ag with all four types, Ir within Rh-foam (type-B), and Pd within Ni foam, see ESI.† The generality of the methods was further tested and proven by preparing type C of Pd-grown@Ni, using a mat of Ni-microfibers – see ESI, Section 1.4, for details.†

2.3. Catalysis

Reductive degradation of methyl orange catalyzed with Pt-NPs in silver composites. The catalytic reaction was performed according to the procedure of ref. 14, modified as follows: 3 mg of selected entrapped Pt catalyst (0.46 μmol Pt) was placed in a 100 mL beaker equipped with a stirrer, to which 60 mL of methyl orange (MO, 4.6 μmol) solution (25.1 mg in 1 L) was added. The reaction started with the addition on 1 mL of $NaBH_4$ (92 μmol) solution (24.3 mg in 7 mL) at 25 °C and 600 rpm. The upper solution was measured spectrophotometrically in constant time intervals. The absorption at 455 nm for each sample was monitored and the reaction kinetics was derived. The molar ratio between the Pt : MO : $NaBH_4$ was kept 1 : 10 : 200 for all composites. For the determination of activation energy in the MO reaction, the above procedure was conducted at different temperatures.

Recycling test was carried out as follows: 1 mL of MO stock solution (125.5 mg in 50 mL TDW) was mixed with 600 μL of $NaBH_4$ solution (48.6 mg in 7 mL TDW) and kept in a close vial in an ice bath. 1 mg of Pt@Ag composite was placed in a 4 mL glass cuvette, filled with 3 mL of TDW and equipped with a magnetic stirrer. The spectrophotometric measurements started with the addition of 160 μL of MO-$NaBH_4$ solution to the cuvette. Once the absorbance of the solution reached 50% of its initial value, another portion of 80 μL of MO solution (1 mL of stock solution + 600 μL of TDW) was added, and this was repeated for additional three times (four in total). Then the upper solution was decanted, the catalyst cleaned with TDW and acetone and the same four-additions process was repeated two additional times.

Reduction of hexacyanoferrate catalyzed with Pt-NPs in silver composites. The catalytic reaction was performed according to the procedure of ref. 15, modified as follows: 1.5 mg of the selected entrapped Pt catalyst (0.23 μmol Pt) was placed in a 4 mL glass cuvette. Afterward, the cuvette was filled with 2.5 mL TDW and 215 μL (46 μmol) of $Na_2S_2O_3$ solution (136 mg in 4 mL TDW), equipped with a stirrer. To this cuvette, 465 μL (4.6 μmol) of $K_3[Fe(CN)_6]$ solution (32.6 mg in 10 mL of TDW) was added. The reaction was carried out at 25 °C and 600 rpm, and followed spectrophotometrically at a fixed wavelength of 425 nm. The molar ratio between the Pt : $K_3[Fe(CN)_6]$: $Na_2S_2O_3$ was set to 1 : 20 : 200 for all composites. Recycling test was carried out as follows: 1.5 mg of Pt@Ag composite was placed in a glass cuvette, filled with 2.5 mL of TDW and equipped with a magnetic stirrer. The spectrophotometric measurements were performed at a fixed wavelength of 425 nm. 215 μL of $Na_2S_2O_3$ solution (136 mg in 4 mL) were added to the cuvette followed by the addition 230 μL of $K_3[Fe(CN)_6]$ stock solution (32.6 mg in 5 mL), after which the spectrophotometric measurement started. At the end of each cycle, the upper solution was decanted and the catalyst was washed with acetone and water.

Electrocatalytic hydrogen oxidation reaction (HOR) with Pd-NPs in Ni fibers. The electrochemical characterization measurement was performed with a three-electrode rotating disk electrode (RDE) placed inside a five-compartment water-jacketed glass cell using WaveDriver potentiostat (from Pine Instrument, USA) at room temperature (25 ± 0.2 °C). A glassy carbon rotating disk electrode of diameter 5 mm was used as a working electrode, Pt wire was used as a counter electrode, and Hg/HgO was used as a reference electrode (4.24 M KOH). The electrodes were procured from Pine Instruments, USA. The inks were prepared by mixing 5 mg catalyst, 1 mL de-ionized water, 2 mL isopropyl alcohol, and 4.76 μL Nafion® ionomer *via* sonication for 30 min. The required amount of ink was loaded on the glassy carbon tip and dried in an air atmosphere to get the metal loading of *ca.* 13 μg per Pd per cm^{-2}. For the control experiment, the response for fibers of Ni (decorated with NiO) was also measured. The electrolyte was first purged with Ar gas to remove excess O_2, and then cyclic voltammograms (CVs) were first recorded in an Ar-saturated 0.1 M KOH solution. After CV, the electrolyte solution was purged with H_2 until the open circuit potential was stabilized, and then the linear sweep voltammograms (LSVs) are recorded at a rotation speed of 1600 rpm to register the HOR polarization. The potential of the reference electrode was calibrated *vs.* reversible hydrogen electrode (RHE), and the electrochemical results were reported against RHE.

3. Results and discussion

3.1 Terminology and notations

For clarity of the presentation of the results and discussion, here are the notations and terminology of the four main types of metallic hybrids we present (see Experimental details):

Type-A, denoted M1@M2: entrapment of M1-NPs within porous M2.

Type B, denoted M1@M2-foam: entrapment of M1-NPs within a foam of M2. The porous M2 and the M2 foam are different materials, as explained below.

Type C, denoted M1-grown@M2: *in situ* growth of M1 inside porous M2.

Type D, denoted M1-grown@M2-foam: *in situ* growth of M1 inside M2-foam.

In what follows, we shall describe in detail the four types for platinum entrapped in silver, adding main comparative comments regarding the other metal systems – Au within Ag, Ir within Rh, and Pd within Ni; further full details for these additional systems are collected in the ESI.†

3.2 The syntheses the doped metals

After intensive preliminary tests, the chosen optimal load was found to be around 3 wt% of Pt-NPs (see ESI Section 2.1† for discussion comments of their synthesis). This loading also applies to all other bimetallic composites described below and was ensured by careful testing of the supernatant solutions of the various syntheses. The entrapping matrices were either aggregated Ag (termed here porous Ag) or silver foam (so-termed), which are prepared differently. As already mentioned in the introduction, the synthetic approach towards the entrapment of Pt-NPs within Ag (Pt@Ag – type A and Pt@Ag-foam – type B) was based on the principles of the methodology of molecularly doped metals and its extension to functional NPs entrapped within metals. For type-A, the reductive entrapping reaction is:

$$2AgNO_{3(aq)} + H_3PO_{2(aq)} + H_2O_{(l)} \Rightarrow 2Ag_{(s)} + H_3PO_{3(aq)} + 2HNO_{3(aq)},$$

in the presence of Pt-NPs. The reducing agent, hypophosphorous acid, is a modification of the previously widely used sodium hypophosphite in other syntheses of dopant@metal,[16,17] which was found to be optimal for the entrapment of the NPs. Gradual reduction and aggregation of the silver then occur, during which the NPs are tightly entrapped within the formed matrix.

For type B, the silver foam, the reducing agent of choice is sodium borohydride, $NaBH_4$.[9] The reason is the dual role of this agent – it is used both as a reducing agent for the Ag^+ cations, and as a foaming agent since it evolves hydrogen gas while reacting with the aqueous reaction medium. Therefore, in this case, the reducing agent is used in an excess of 5 molar ratio compared to the $AgNO_3$. The entrapping reaction carried out in the presence of Pt-NPs is:

$$8AgNO_{3(aq)} + BH_{4(aq)}^- + 3H_2O_{(l)} \Rightarrow 8Ag_{(s)} + B(OH)_{3(aq)} + 7H^+_{(aq)} + 8NO_{3(aq)}^-,$$

and the foaming is affected by:

$$BH_{4(aq)}^- + 4H_2O_{(l)} \Rightarrow B(OH)_{4(aq)}^- + 4H_{2(g)}.$$

While in the above-described types A and B the *a-priori* preparation is of the Pt-NPs, in types C and D the *a-priori* preparation is of the porous and foamy Ag matrices. Here the precursor metal salt is adsorbed within the pre-prepared matrix reaching all of internal pores surface, which is then reduced upon contact with the Ag to metallic Pt:

$$4Ag_{(s)} + Pt_{(aq)}^{4+} \Rightarrow Pt_{(s)} + 4Ag_{(aq)}^+.$$

PVP is added too in order to affect separation between the Pt particles to be formed, avoiding a continuous Pt layer.

We move next to the other bimetallic systems: for the gold within silver materials types A and B, gold NPs (very widely studied and attracting a lot of attention in the last decades[18]) were synthesized with PVP as a capping agent (similarly to the synthesis of Pt-NPs)[19] according to:

$$8Au_{(aq)}^{3+} + 3BH_{4(aq)}^- + 9H_2O_{(l)} \Rightarrow 8Au + 3B(OH)_{3(aq)} + 21H_{(aq)}^+.$$

After the cleaning of the NPs (average size 1.9 nm) from the PVP they were entrapped within porous Ag and Ag foam using H_3PO_2 and $NaBH_4$ as reducing agents, respectively, as described for the entrapment of Pt-NPs. For the *in situ* Au-grown composites, the Ag matrices were used for the generation of the Au in the matrix's pores by the following reaction:

$$3Ag_{(s)} + Au_{(aq)}^{3+} \Rightarrow Au_{(s)} + 3Ag_{(aq)}^+.$$

Due to the high surface area of the metallic foams (see next section), which makes them potentially useful for catalytic applications, two additional type-B doped foams were prepared, Ir@Rh-foam and Pd@Ni-foam (average NPs sizes of 1.7 nm and 2.8 nm, respectively). Ir NPs were synthesized according to:[20]

$$8Ir_{(aq)}^{3+} + 3BH_{4(aq)}^- + 9H_2O_{(l)} \Rightarrow 8Ir + 3B(OH)_{3(aq)} + 21H_{(aq)}^+,$$

which were entrapped within a foam Rh matrix according to:

$$8Rh_{(aq)}^{3+} + 3BH_{4(aq)}^- + 9H_2O_{(l)} \Rightarrow 8Rh_{(s)} + 3B(OH)_{3(aq)} + 21H_{(aq)}^+.$$

Using an excess of X15 mole BH_4^- for the foaming. Likewise, for Pd@Ni-foam, the Pd-NPs stabilized with PVP, were synthesized according to:[21]

$$4Pd_{(aq)}^{2+} + BH_{4(aq)}^- + 3H_2O_{(l)} \Rightarrow 4Pd + B(OH)_{3(aq)} + 7H_{(aq)}^+.$$

In this case, the NPs were entrapped with the PVP coating because its removal caused their aggregation. However, the PVP was washed after the entrapment. The entrapping metallic Ni foam was prepared, as in the previous composites, by using $NaBH_4$ as a reducing agent:

$4Ni_{(aq)}^{2+} + BH_{4(aq)}^{-} + 3H_2O_{(l)} \Rightarrow 4Ni_{(s)} + B(OH)_{3(aq)} + 7H_{(aq)}^{+}$.

An excess of 10 times mole BH_4^- was used for foaming as described above.

Last but not least, in order to further demonstrate the generality of the approach to other porous surface area metallic supports, another type of Ni doped with palladium was prepared, using this time electrospun Ni fibers, about 250 nm in diameter and 1 micron long, synthesized by hydrogen reduction from NiO mats (provided generously by the authors of ref. 40). On these Ni fibers, Pd was *in situ* grown to form Pd-grown@Ni-fiber (similar to type C), according to:

$$Ni_{(s)} + Pd_{(aq)}^{2+} \Rightarrow Pd_{(s)} + Ni_{(aq)}^{2+}.$$

As described in the next section, the Ir–Rh and Pd–Ni syntheses are accompanied by some oxidation. Customarily, prior to the use of these metals for catalysis, they undergo a hydrogen reductive activation process.

3.3 Material characterizations – the four Pt-in-Ag systems

We focus in this section on the materials characterization of the platinum within silver systems, as the leading case. The full material characterization of all other bimetallic M1@M2 systems, along with comparison to the observations summarized here, appear in the ESI, Section 2.3.†

Scanning electron microscopy (SEM). Extra high reolution (XHR)-SEM images of all four types Pt-in-Ag systems described in Section 3.1 are shown in Fig. 1 (types A and B, Pt entrapped in porous Ag and in Ag foam), and in Fig. 2 (types C, and D, Pt grown in porous Ag and in Ag foam); the pure Ag matrices are shown for comparison in Fig. S2, ESI, Section 2.† A hierarchical structure is seen for both matrices: on the largest scale, the powder is composed of tens of microns open, porous aggregates, which in turn are built from smaller tight aggregated Ag down to sub-micron levels, and, as we shall see below, XRD reveals the finest nanometric scale of the Ag crystallites that form the entrapping cages of the Pt. It is clearly seen – Fig. 1 – that the tight Ag building blocks of the Ag foam are smaller than those of the porous Ag, and that the foam has a net-like structure composed of the smaller particles. The difference in the morphologies reflects the different synthetic processes: the porous Ag is obtained with a small excess of H_3PO_2 (ratio of 1 : 1.2) resulting in a slow reduction (8 hours), which encourages the growth process over the nucleation. On the other hand, the foam is obtained by reduction with a larger excess (ratio of 1 : 5) of a stronger reducing agent, $NaBH_4$, during which an H_2 gas is being evolved, thus resulting in smaller particles and foam-like structure. It is also noticed that the Ag aggregates of Pt@Ag are composed of two populations: smaller undefined aggregates and larger highly ordered aggregates of triangular and hexagonal form. The ordered aggregates are formed due to the presence of PVP in the synthesis, which binds selectively to a certain facet in the crystal (⟨100⟩ in the case of Ag), directing its growth on other facets, creating the observed shapes.[22] In the

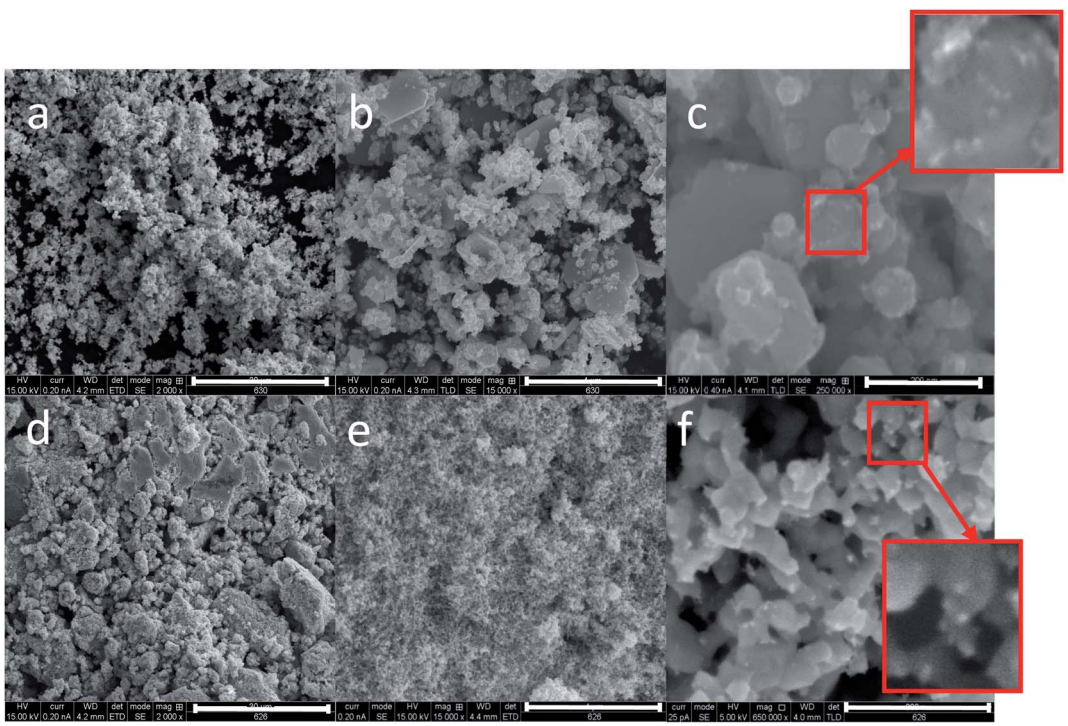

Fig. 1 XHR-SEM images of entrapped platinum NPs within silver composites: (a–c) Pt@Ag, (d–f) Pt@Ag-foam. Pt-NPs of approximately 2 nm can be seen inside the enlarged squares. Bars: (a and d): 30 μm; (b and e): 4 μm; (d and f): 200 nm.

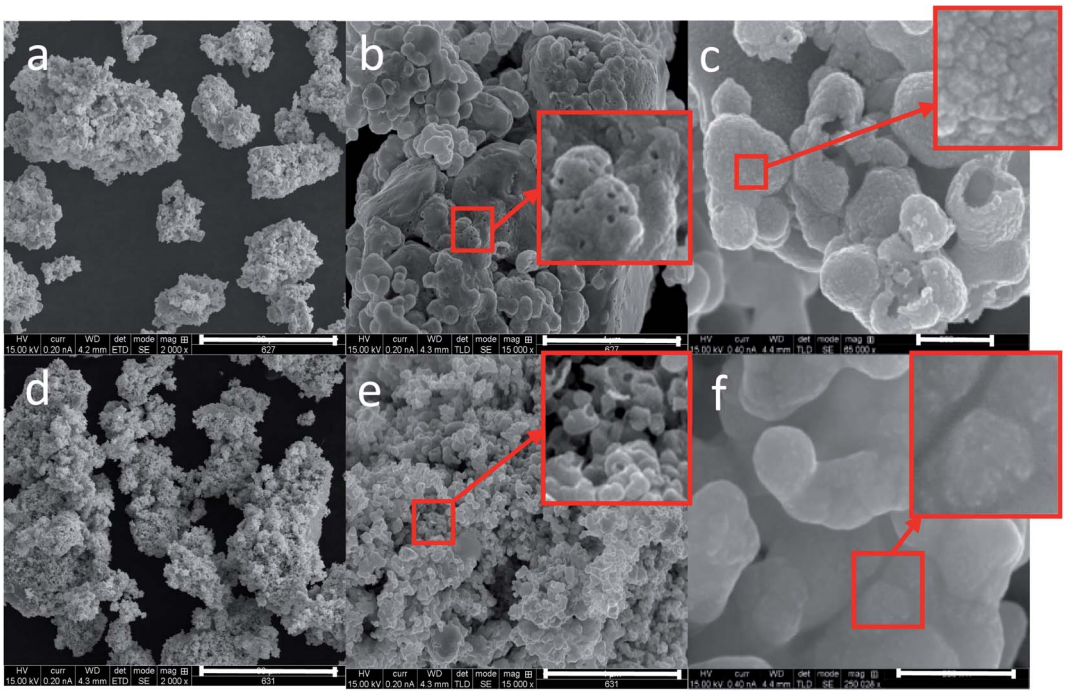

Fig. 2 XHR-SEM images of composites of *in situ* grown platinum within silver: (a–c) Pt-grown@Ag, (d–f) Pt-grown@Ag-foam. Pt particles and islands can be seen inside the enlarged squares. Bars: (a and d): 30 μm; (b and e): 4 μm; (d and f): 200 nm.

Pt@Ag-foam composite, these two populations are not observed, regardless of the presence of PVP in the synthesis, since the reduction of the matrix is much faster, causing a preference to the nucleation process over the growth of the matrix's aggregates.

In both composites, it can be seen that the largest magnifications (c) and (f) reveal a certain roughness of the surface compared to their blanks in Fig. S2.† The main reason for this roughness, as displayed in the magnified squares, is the entrapment of the Pt nanoparticles of approximately 2 nm. The most prominent feature in the case of the Pt grown composites (types C and D, Fig. 2) are the cavities in the silver matrices of the composites (seen in the red squares). These cavities are formed by the *in situ* reduction of the Pt ions by the silver matrix (not seen in the blank Ag matrices – Fig. S2†). In the case of the foam composite (f), the Pt appears almost as discrete and fine particles on the surface, while in the Pt-grown@Ag composite they appear as separated crude islands (c). We propose that this difference is due to the larger surface area of the foam, which enables better dispersion.

X-ray diffraction (XRD). XRD measurements are needed in order to determine the size of the most elementary building blocks in the hierarchical structure, the Ag nanocrystallites, as well as the effect of the different synthetic routes on their size. The XRD spectra are presented in Fig. S3,† which exhibits the characteristic peaks of Ag,[23] corresponding to its typical FCC facets. Splitting is seen in some of the high angles, probably due to both Cu Kα1 and Cu Kα2 X-rays.[24] The Pt crystalline phases are not detected since their quantity is very small compared to the Ag (about 3 wt%), and since they are very small in size (about 2 nm, Fig. S1†). Using Scherrer's equation, the XRD data provides the crystal sizes of the Ag in the various composites, which are summarized in Table 2.

It is seen that the pure silver foam and its composites (types B and D) have smaller elementary crystal sizes compared to the porous silver analogs (types A and C). This data also agrees with the SEM images (Fig. 1, 2 and S2†). The reason for this difference is again reflecting the difference in the synthetic conditions: the use of $NaBH_4$ in a large excess promotes more nucleation centers in the foam composites compared to the non-foam composites, thus resulting in smaller Ag crystals.

It is also seen that the silver in all composites has smaller crystal sizes compared to their Ag pure matrices. This trend was also observed in molecular dopant@metal composites, and the rationalization has been that the dopant inhibits the crystal growth of the matrix through reversible adsorption interactions between the dopant and the surface of the growing matrix nanocrystallite.[7]

Surface area and porosity. Another feature that implies directly on the structure of the composites is their surface area

Table 2 Physical properties of platinum within silver composites

Composite	Ag crystal size (nm)	Surface area ($m^2\ g^{-1}$)	Total pore volume ($cm^3\ g^{-1}$)
Porous Ag	93.4	0.36	0.39 ± 0.06
Foam Ag	42.3	2.36	1.79 ± 0.04
Pt@Ag	43.8	3.79	0.39 ± 0.02
Pt@Ag-foam	17.3	9.74	0.59 ± 0.05
Pt-grown@Ag	51.1	1.03	0.40 ± 0.10
Pt-grown@Ag-foam	37.3	2.78	0.58 ± 0.07

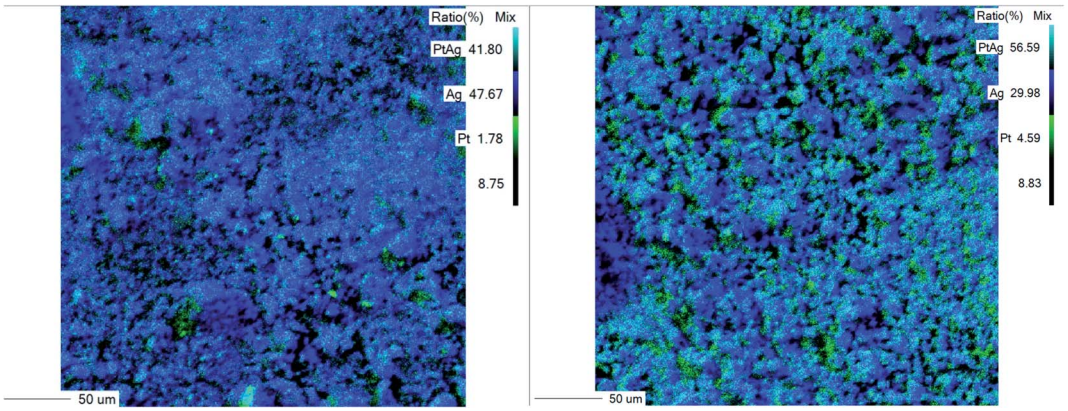

Fig. 3 WDS maps of platinum within silver composites: right – Pt@Ag; left – Pt-grown@Ag. Green, light blue and deep blue represent areas with Pt, Pt–Ag and Ag respectively. Bars: 50 μm.

and porosity. These were determined from the adsorption/desorption isotherms of N_2 physisorption on the surface of the composites. The surface area, as well as the total pore volume values, are summarized in Table 2. As expected, all foams have higher surface areas compared to the aggregated porous matrices. It is also noticeable that the entrapment of Pt NPs significantly increases the surface area of both the porous matrix and the foam. It is most probably due to the combined effect of the decrease in the particle sizes which build the Ag matrices (Table 2), with a contribution to the surface area from

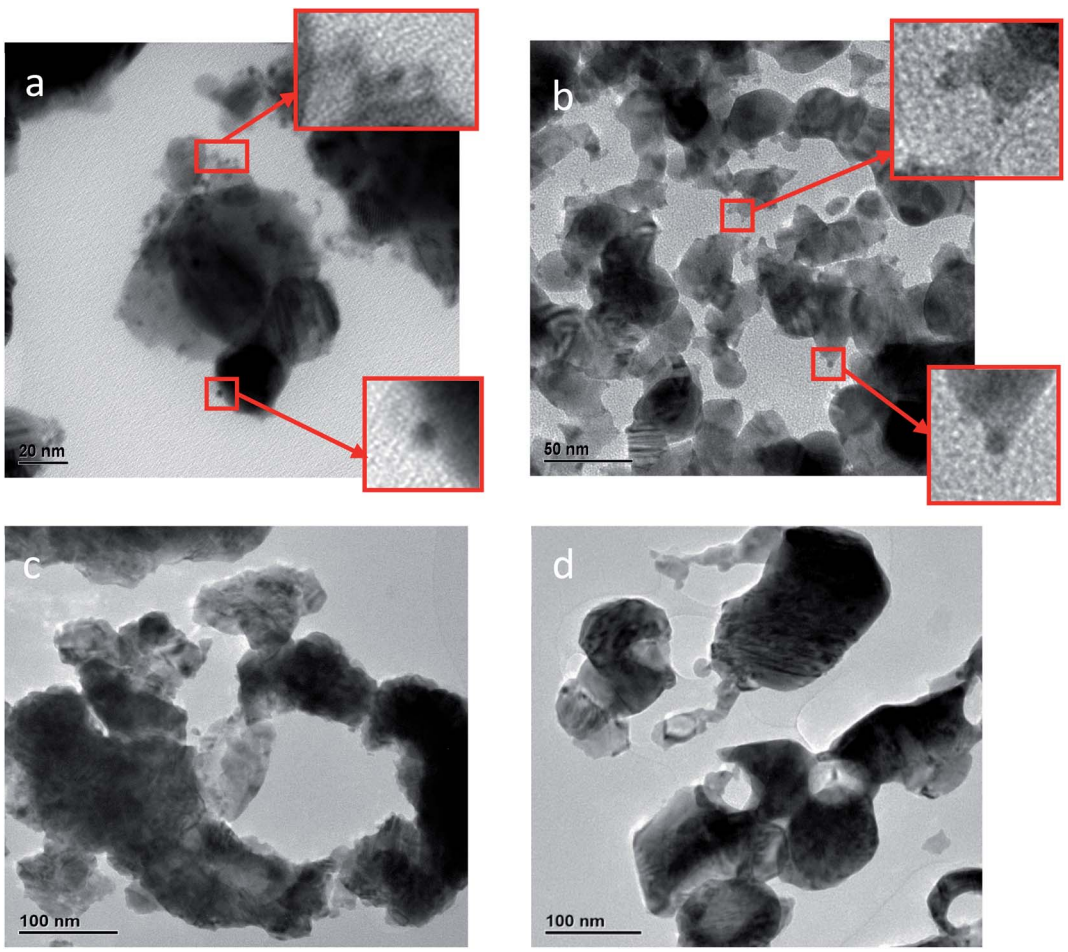

Fig. 4 HR-TEM images of entrapped platinum within silver composites: (a) Pt@Ag. (b) Pt@Ag-foam. Pt NPs can be seen in the squares of (a) and (b). (c) Pt-grown@Ag. (d) Pt-grown@Ag-foam.

the Pt NPs themselves, which have a large surface-area/volume ratio. The surface area increase is also seen for the Pt-grown@Ag composite, although the effect is smaller, but for the Pt-grown@Ag-foam, the surface area remains almost unchanged. We attribute the smaller effect in the case to possible blocking of the narrow micropores which contribute most to the surface area: while entrapment leaves these micropores unaffected, the growth process has properties of coating of the surface, and hence its blocking effect. On the other hand, the Ag matrix decomposition during the reduction of the Pt ions in the Pt-grown composites, creates voids and cracks in the matrix thus, increases the surface area. Subsequently, these two effects compensate each other, so only a slight change in the surface area is observed. The values of the total pore volumes of the materials are summarized in Table 2 as well. As expected from the synthetic routes, the pore volume of the pure foam is significantly higher than the pure Ag porous matrix. Almost no change in the pore volume is observed when the porous Ag is loaded with Pt (Pt@Ag and Pt-grown@Ag), but in the foam composites, a decrease in the pore volume is observed, apparently due to blocking of pore entrances.

Electron dispersive spectroscopy (EDS) and wavelength-dispersive X-ray spectroscopy (WDS). We recall that WDS uses the same physical principles as the EDS, except that contrary to EDS that collects the whole X-ray emitted spectrum, WDS collects one wavelength at a time, which renders this method of much higher elemental resolution. The first step in 2D-WDS analyses is to perform routine 2D-EDS analyses in order to detect the elements existing in the sample. Such 2D-EDS maps are collected in Fig. S4† and show an important result, namely, that there is a good distribution of the Pt dopant with no significant phase separation. The 2D WDS maps of the elemental distribution of Pt@Ag and Pt-grown@Ag in a scanned area of about 300 × 300 μm are shown in Fig. 3, and it is seen that the resolution is indeed much better, allowing observation of the distribution of very fine Pt domains.

It is seen in Fig. 3 that in the Pt@Ag composite, there are smaller Pt particles compared to the Pt-grown@Ag composite. This observation corresponds with the experimental procedure, as well as with the SEM images (Fig. 1 and 2) since the Ag in the Pt@Ag composite stabilizes discrete 2 nm Pt nanoparticles, while the Pt-grown@Ag composite is composed of thicker, cruder Pt islands layer. The roughness of the foams made it technically difficult to apply the WDS analysis; however, EDS provided the needed chemical analysis (Fig. S4†).

The metal–metal interface – transmission electron microscopy (TEM). High-resolution TEM (HR-TEM) and scanning TEM (STEM) and their coupling to EDS elemental analysis served for the characterization of the metal–metal interface. Fig. 4(a and b) show the TEM structures of Pt@Ag and Pt@Ag-foam composites on a nanometric scale. The way that the Pt NPs are embedded in the Ag matrix can be seen in the enlarged squares. Comparing the

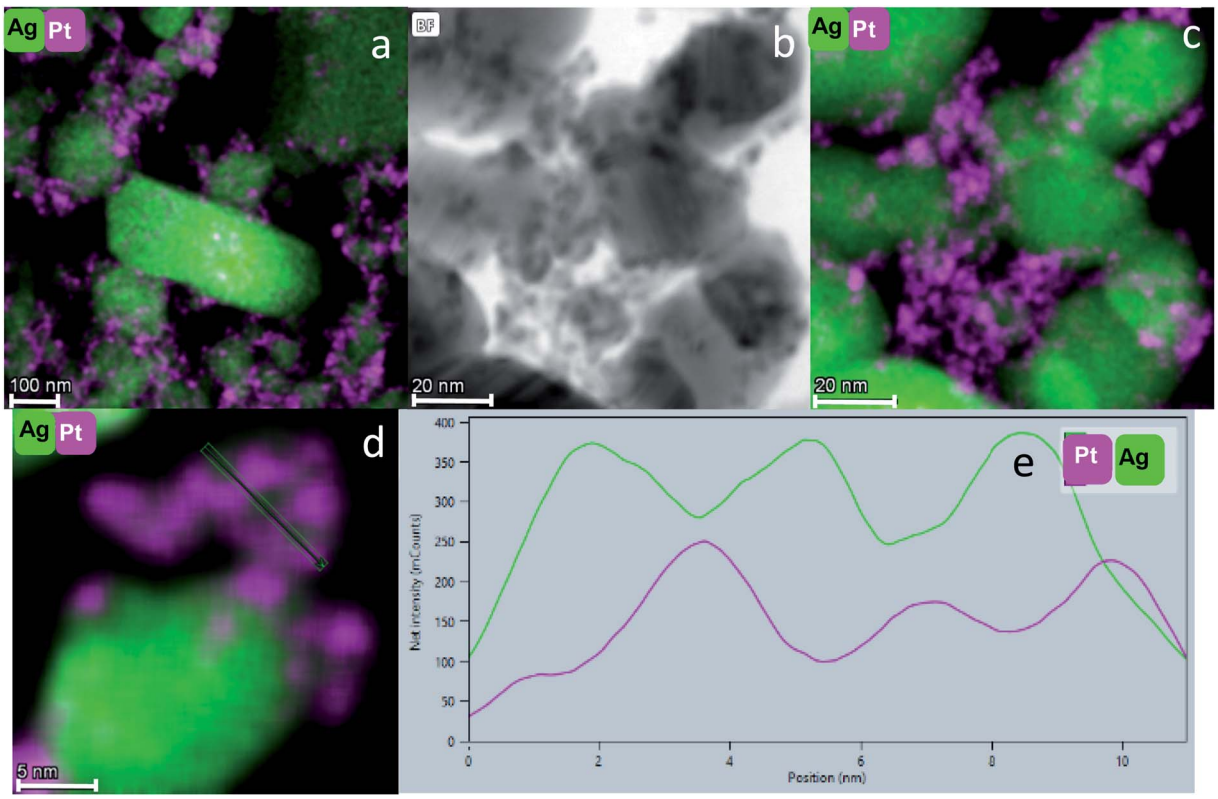

Fig. 5 (a) STEM – EDS elemental mapping of Pt@Ag (bar: 100 nm). (b) STEM image of Pt@Ag and its corresponding EDS elemental mapping shown in (c). (d) EDS elemental mapping of Pt@Ag and (e) a profile of the elemental composition along the marked line in (d). Pink: Pt, green: Ag. Bars: (b and c): 20 nm, (d): 5 nm.

interface of the NPs with the Ag matrix in the two composites, it is seen that there is a larger contact area between these metals in the foam composite. The Ag crystals on which the Pt particles are found in the foam composite look somewhat elongated towards the Pt tip (b), while in the Pt@Ag composite (a) the Pt particle is placed on an almost planar Ag surface, resulting in a more exposed Pt surface. An explanation of this difference is based on the structures of the two Ag matrices – in the porous Ag (Pt@Ag) the building blocks of the Ag are much larger compared to the Ag-foam (Table 2), and therefore in the Pt@Ag case, the energetically preferred contact configuration is maximizing the interaction between flat areas of both the Pt and the Ag crystal faces.

The TEM images of the grown platinum within silver composites (Pt-grown@Ag and Pt-grown@Ag-foam), on the other hand, look quite different. The images, shown in Fig. 4(c and d) reveal mainly the structure of the Ag matrix, but it is not obvious to the naked eye where the Pt is placed. Cavities and holes are seen on the Ag aggregates surface in this case, and the Ag matrix structure cross section looks as if it was corroded. This is due to the decomposition of the Ag during the formation of the Pt. Typical d-spacings of about 2.35 Å and 2.29 Å for silver and platinum, respectively, were measured from TEM images. Although these values support the assignments made, due to their close values, the additional methods described here were used.

STEM coupled with EDS is probably the most informative method for our purpose: Fig. 5(a) shows the fine dispersion of the Pt NPs in the Ag matrix in the Pt@Ag composite. Fig. 5(b) shows a STEM image at a higher resolution and (c) is its elemental mapping. It can be seen that the NPs in (b) indeed overlap with the Pt in the (c). A similar analysis is shown in Fig. 6(a and b) for the Pt@Ag-foam composite.

Fig. 5(d) shows clearly the embedding of the Pt-NPs in the silver matrix in a higher magnification. An important observation is made by following the elemental composition along the scanning line shown in Fig. 5(d): The composition profile Fig. 5(e) shows that with each maximum of the Pt counts (pink), there is a minimum of Ag counts (green). Namely, the Pt NPs are closely embedded in kind of a 'bowl' shape cavities of the Ag matrix. The Pt and Ag are overlapping in their interface, but each of the phases is separate and they do not blend or form an alloy. A similar analysis was made for the entrapment in foam – Fig. 6(c and d): the Pt NPs are wrapped more intimately by the Ag compared to the case of Pt@Ag (confirming the primary TEM observation) and as a consequence, the increase in the counts of the Pt along the marked area does not correspond with a decrease in the Ag counts (Fig. 6(d)). Fig. 7 shows the results of

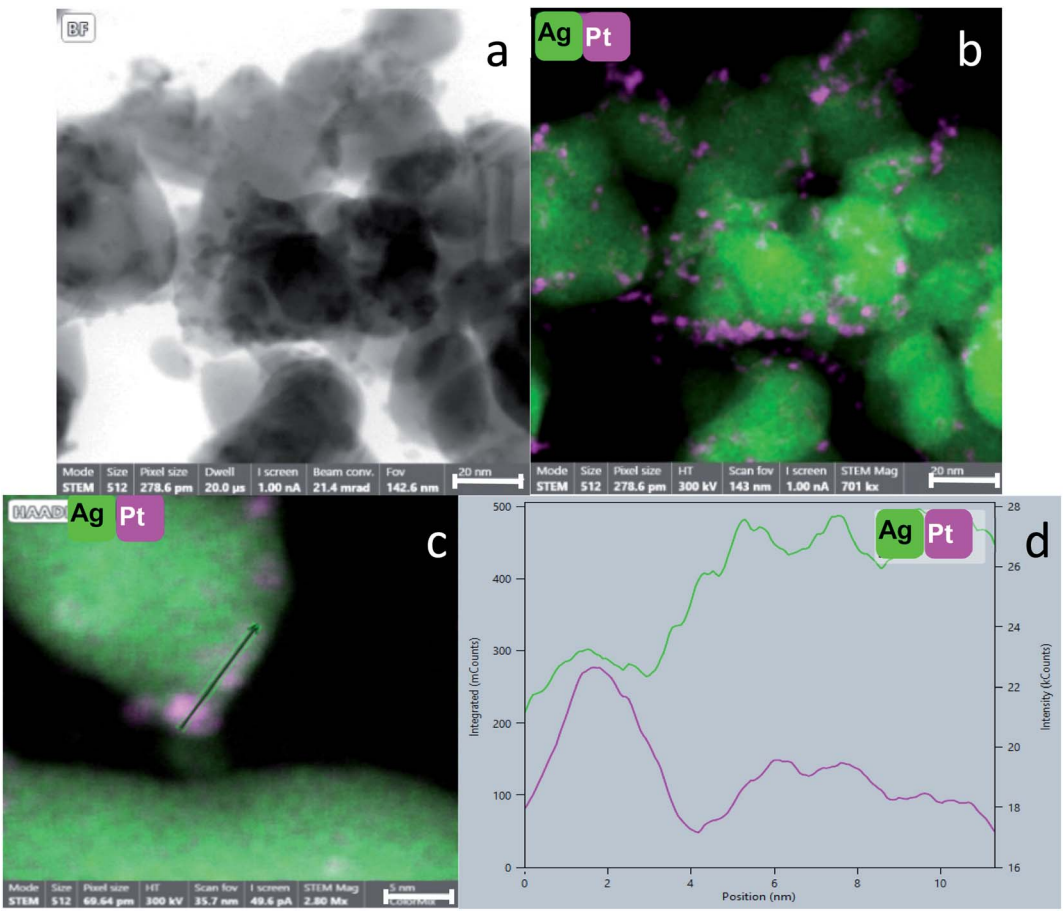

Fig. 6 (a) STEM image of Pt@Ag-foam. Its corresponding EDS elemental mapping is shown in (b). (c) EDS elemental mapping of Pt@Ag-foam and (d) a profile of the elemental composition along the marked line in (c). Pink: Pt, green: Ag. Bars: (a and b): 20 nm, (c): 5 nm.

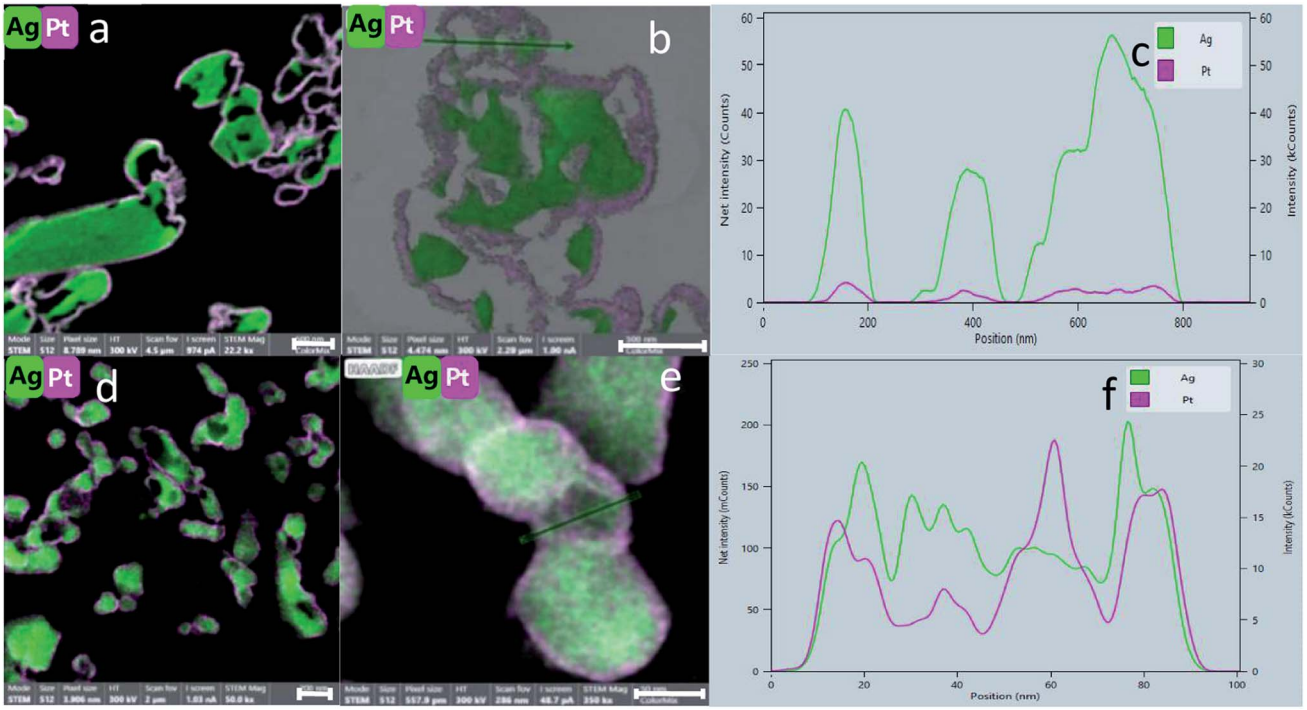

Fig. 7 (a) EDS elemental mapping of Pt-grown@Ag. (b) EDS elemental mapping of Pt-grown@Ag and (c) a profile of the elemental composition along the marked line in (b). (d) EDS elemental mapping of Pt-grown@Ag-foam. (e) EDS elemental mapping of Pt-grown@Ag-foam and (f) a profile of the elemental composition along the marked line in (e). Pink: Pt, green: Ag. Bars: (a), (b): 500 nm, (d): 200 nm, (e): 50 nm.

this analysis for *in situ* grown composites – Pt-grown@Ag and Pt-grown@Ag-foam. The figure clearly reveals the coating nature which results from the *in situ* generation of the Pt that is completely different from the Pt distribution and morphology in the entrapping composites.

The main difference between the two Pt-grown composites is the thickness of the grown Pt – in the Pt-grown@Ag the Pt is much thicker, forming in fact partial coating (of a magnitude of order of about 100 nm thick), while in the Pt-grown@Ag-foam the coating in more delicate (about 10 nm). This difference originates from the difference in the surface areas, which in the foam matrix is much higher, that is, more area is available to be covered by the same amount of Pt, resulting in the thinner coating. Fig. 7(e and f) shows this difference with the composition profiles: In Fig. 7(f) it is seen that the peaks of the elements are not overlapping completely – Pt increases before the Ag, indicating that there are some areas that are distinctively only Pt. The Pt layer in the Pt-grown@Ag-foam composite is composed of Pt islands and particles, and its thickness is not constant in all covered areas.

3.5 Catalysis

The aims of the catalysis study were dual: First, catalytic metal NPs have traditionally been supported on ceramic, glassy and polymeric supports, *but never on high surface area metallic supports*; we demonstrate here the applicability of this new materials-type support. Second, we use the catalytic reactions to tell us more about the structure and properties of these metallic composites, and about the resulting differences between the four types developed here.

Catalysis using the Pt in silver composites

Methyl Orange reductive catalytic degradation. The importance of this reaction is in the field of water pollution:[25] azo dyes such as Methyl Orange (MO) are widely used in various industries (cosmetics, food, textile, *etc.*), despite the fact that they are toxic and with low biodegradability; an effective method for their degradation is therefore needed. Following the observations that Pt-NPs catalyze reductive degradations of such compounds,[14,25,26] we tested the ability of our composites to catalyze the MO reductive degradation to sodium sulfanilic acid and *N*,*N*-dimethyl-*p*-phenylenediamine:

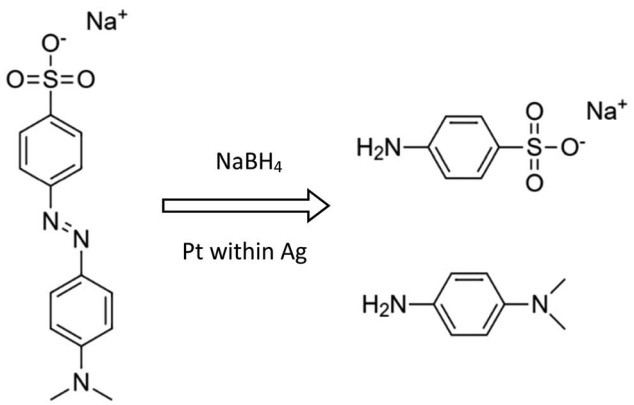

and catalysis was indeed found to be affected. The reaction is followed spectroscopically by the decline in time of MO

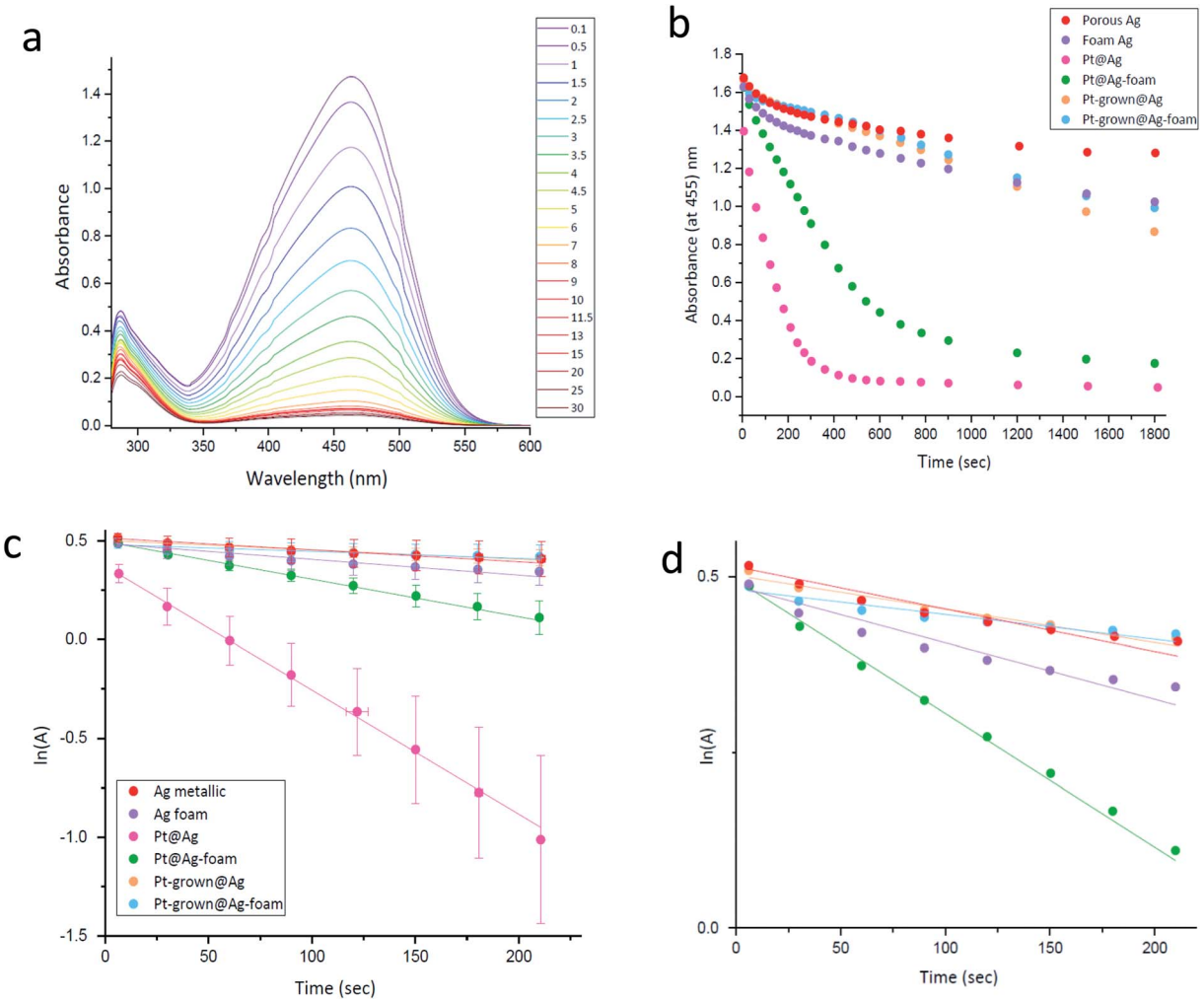

Fig. 8 (a) Methyl Orange reductive degradation catalyzed by Pt@Ag composite. The time steps in the column are in minutes. (b) Methyl orange catalytic reductive degradation by different platinum within silver composites. (Each graph is an average of 9 measurements). (c) Methyl orange catalytic reductive degradation by Pt within Ag composites, presented as pseudo first order kinetics-full scale. (d) The 0.0–0.5 ln(A) range of (c).

Table 3 Rate constants and half-lives of the platinum within silver catalyzed reductions

	Porous Ag	Ag foam	Pt@Ag	Pt@Ag-foam	Pt-grown@Ag	Pt-grown@Ag-foam
MO reduction rate constant $\times 10^{-3}$(sec^{-1})	0.60 ± 0.05	0.80 ± 0.08	6.3 ± 0.1	1.91 ± 0.06	0.47 ± 0.05	0.35 ± 0.04
MO, $t_{1/2}$ (sec)	1200 ± 100	900 ± 100	110 ± 2	360 ± 10	2000 ± 200	1500 ± 100
$Fe(CN)_6^{3}$ reduction rate constant $\times 10^{-3}$ (sec^{-1})	2.970 ± 0.003	2.050 ± 0.007	15.4 ± 0.3	5.64 ± 0.02	1.550 ± 0.009	6.980 ± 0.006
$Fe(CN)_6^{3}$, $t_{1/2}$ (sec)	233.4 ± 0.2	338 ± 1	44.9 ± 0.9	122.9 ± 0.4	447 ± 3	99.31 ± 0.08

absorbance. The full set of spectra for Pt@Ag (type A) is collected in Fig. 8(a), and these were converted to kinetic profiles at 455 nm for all of the four types in Fig. 8(b) (including the Ag blanks). It is seen that there is a strong catalytic activity for the types A and B – Pt@Ag and Pt@Ag-foam. It is also seen, on the full-time scale of the figure, that the Ag porous matrix has some weak catalytic activity contribution – the pure Ag foam is more active than the pure porous Ag due to its larger surface area and smaller average particle size, and this activity is only slightly affected by growing Pt on it.

Since $NaBH_4$ is taken in large excess and since the catalyst is not consumed, a pseudo first-order kinetics analysis with respect to the MO concentration (the absorbance, A) was carried out for short times. The results are presented in Fig. 8(c and d): (c) is the full scale for all the composites and (d) is in the expanded ln(A) range of 0.0–0.5. It is seen that the pseudo first-order assumption is fairly good, and the kinetic parameters are

collected in Table 3. It confirms the high activities of Pt@Ag and Pt@Ag-foam – an increase in factors of 10.5 and 2.3 in the rate constants compared to the blanks, respectively.

The activity order of the lesser active materials slightly changes to foam Ag > porous Ag > Pt-grown@Ag > Pt-grown@Ag-foam. The *in situ* grown composites, Pt-grown@Ag and Pt-grown@Ag-foam (types C, D) show no increase in the catalytic activity compared to silver, and even a small decrease in the short time scales. This observation highlights the importance of the morphology of the metallic catalyst in affecting its activity: while the pre-prepared Pt-NPs are active in this reaction, the grown Pt islands that are formed on the surface of the Ag matrix are apparently not energetic enough, that is, with a small number of defects and active sites needed to enhance this reaction. Since the pure foam matrix is more active than the pure porous Ag, one might expect that the combined activity with Pt NPs will result in an activity order of Pt@Ag-foam > Pt@Ag, while the opposite is true. It implies that the NPs in the Pt@Ag are more exposed to perform the catalysis, while in the foam they are more buried in the matrix. This observation is indeed supported by the HR-TEM and STEM results described above (Fig. 4–6). The catalytic reduction of MO with Pt@Ag was also monitored at different temperatures in the range of 5–30 °C, in order to calculate the activation energy, using the Arrhenius equation. Fig. 9(a) shows that the reaction complies with this equation and the value of the activation energy derived from it is 88 ± 9 kJ mol^{-1}. This value indicates that the reaction is not controlled by the diffusion of the substances (usually resulting in activation energies smaller than 21 kJ mol^{-1}[27]), but rather a surface-controlled reaction.[26,28] Recyclability for three cycles was tested and the results are shown in Fig. 9(b). It is seen that cleaning between the cycles preserves the activity, but with a slight decrease in the reaction rate.

The catalytic reduction of hexacyanoferrate reduction. The second Pt-catalytic reaction that was examined is sodium thiosulfate reduction of hexacyanoferrate. The reduction of hexacyanoferrate(III) to ferrocyanide(II), is a well-known model reaction for the examination of NPs catalytic activity,[29] and as

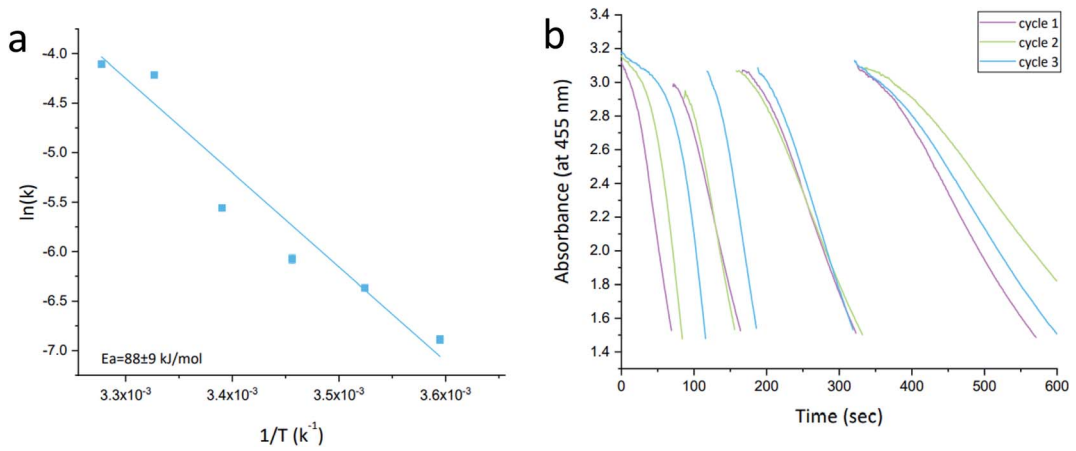

Fig. 9 (a) Arrhenius plot of the reductive degradation of Methyl Orange with Pt@Ag catalyst. The correlation coefficient of the fit to the equation is 0.947. (b) Recycling test of Pt@Ag in the MO reductive degradation reaction. Vertical gaps indicate addition of starting material. Three cycles are shown – see color code.

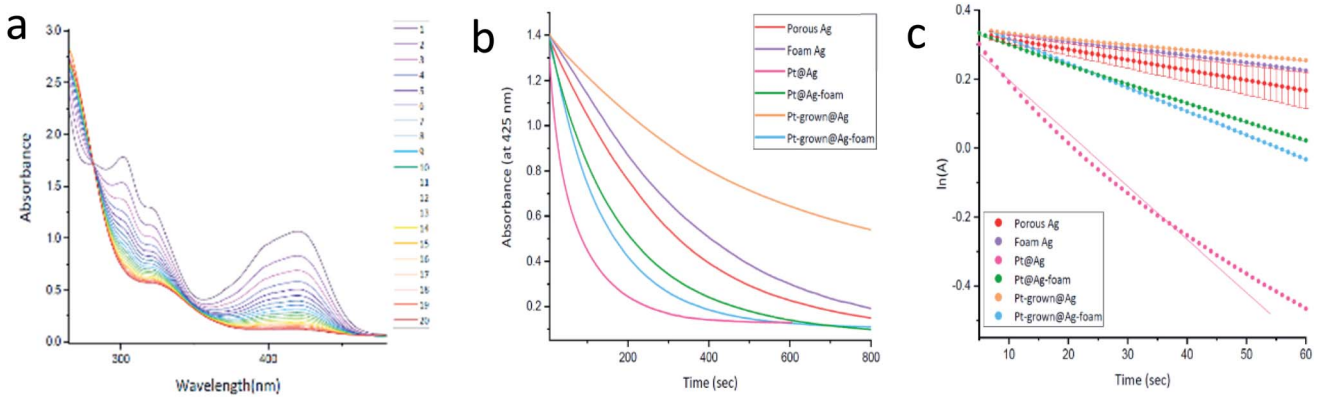

Fig. 10 (a) Hexacyanoferrate(III) catalytic reduction with thiosulfate as the reducing agent and Pt@Ag composite as the catalyst. The interval between each spectrum is 10 seconds. (b) Hexacyanoferrate catalytic reduction by the different platinum within silver composites monitored at 425 nm. Each trend is an average of 8 measurements. (c) Representation of the reaction as pseudo first-order kinetics. Typical error bars are shown for porous Ag.

the previous reaction, has importance in environmental aspects in reducing the hexacyanoferrate's toxicity.[30] This reduction was found to be catalyzed by the platinum within silver composites according to:

$$2Fe(CN)_6^{3-} + 2S_2O_3^{2-} \xrightarrow{\text{Pt within Ag catalyst}} 2Fe(CN)_6^{4-} + S_4O_6^{2-}$$

The reaction was monitored spectrophotometrically, and a typical collection of time-changing absorption spectra is presented in Fig. 10(a) for Pt@Ag (type A). The appearance of the isosbestic point confirms the proposed conversion of the starting material to a single product (unlike the previous reaction). The kinetic profiles of the reactions were monitored at 425 nm for the different composites and of the Ag blanks and the results are shown in Fig. 10(b). It is seen that in this reaction, contrary to the results observed for MO degradation, the Ag pure matrices have significant catalytic activity. However, the Pt@Ag, Pt@Ag-foam and Pt-grown@Ag-foam composites clearly show the catalytic effect of Pt, as they have enhanced catalytic activity compared to their blanks.

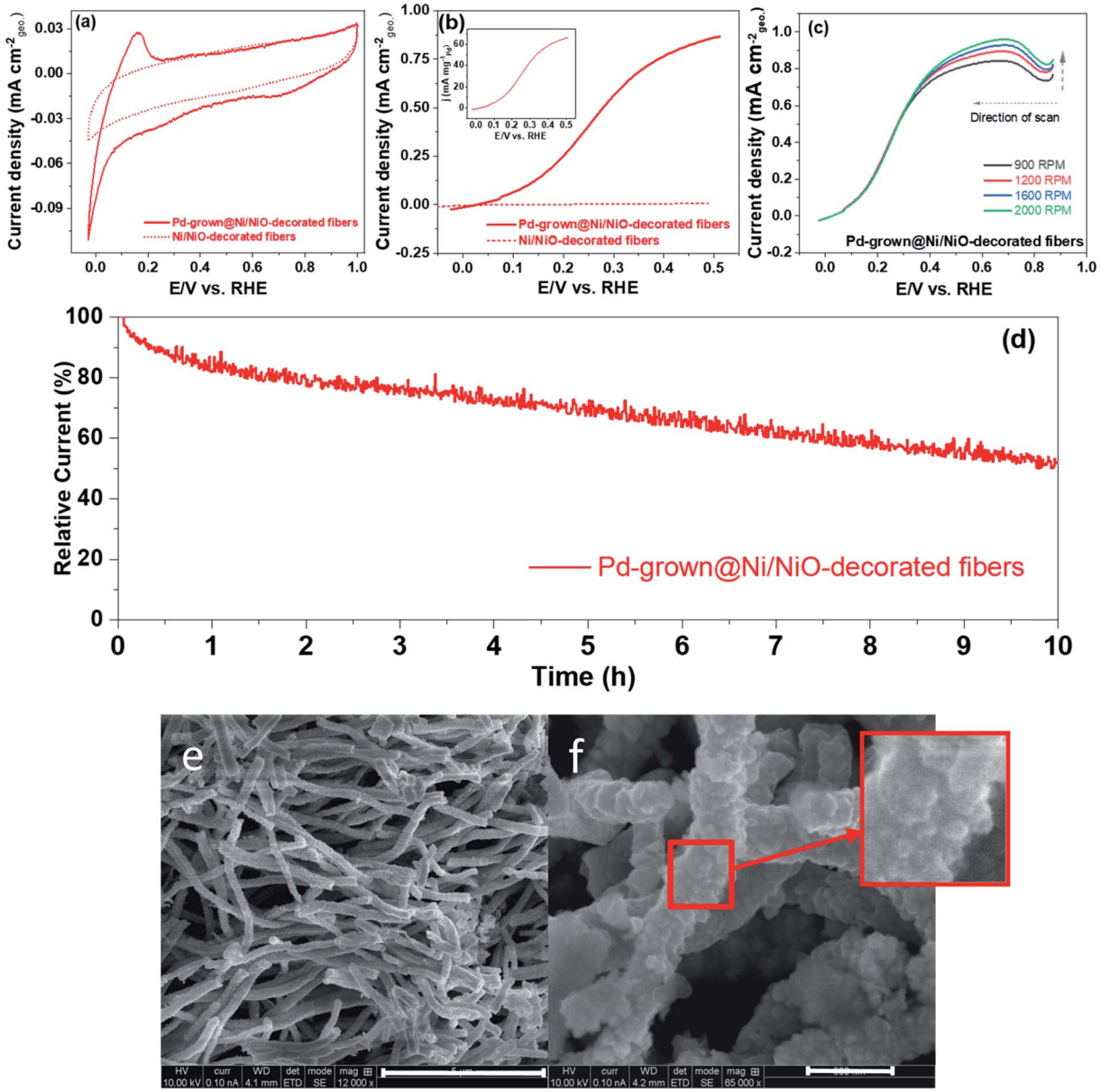

Fig. 11 (a) Cyclic voltammograms (CVs) and (b) hydrogen oxidation polarization curve of Ni/NiO-decorated fibers and Pd-grown@Ni/NiO-decorated fibers. The CV is recorded in argon-saturated 0.1 M KOH electrode at a scan rate of 50 mV s^{-1}, and the HOR polarization curves were recorded in 0.1 M electrolyte at a scan rate of 5 mV s^{-1} with 1600 RPM. Inset to (b) shown mass-normalized activity of Pd-grown@Ni/NiO-decorated fibers, (c) HOR polarization as a function of the rotation speed of the electrode of Pd-grown@Ni/NiO-decorated fibers, and (d) chronoamperometric curves of Pd-grown@Ni/NiO-decorated fibers at 0.37 V in H_2-saturated 0.1 M KOH electrolyte with 1600 RPM. (e) and (f) XHR-SEM images of Pd-grown@Ni-fiber composite. Close-up of the surface morphology is seen in the square. Bars: (e) – 5 μm, (f) – 500 nm.

An exception is Pt-grown@Ag (probably due to some blocking of the active sites of the Ag matrix by the Pt coating). Since the thiosulfate was used in excess, a pseudo first-order kinetic analysis is possible in this case as well and the results are shown Fig. 10(c). The fit to the fastest reaction – Pt@Ag – is slightly curved, but is still good and allows comparison with the other reactions. The kinetic parameters are collected in Table 3. The catalytic activity trends are reserved as in Fig. 10(b): Pt@Ag > Pt-grown@Ag-foam > Pt@Ag-foam > porous Ag > foam Ag > Pt-grown@Ag. The enhancement of the reaction by the entrapped composites is similar to the trend seen for these composites in the MO degradation (the rate constants increase by factors of 5.2 and 2.7 for Pt@Ag and Pt@Ag-foam, respectively), supporting the suggested hypothesis that the Pt available active sites are the governing parameter. Moreover, the close values – same order of magnitude – of the rate constants obtained for the two reactions (the Pt@Ag rate constant in the MO degradation is 6.3 and in the hexacyanoferrate reduction, 15.4) suggests a certain resemblance between the two reactions: both reactions include a transfer of electrons from the donor to the acceptor through the metallic catalyst, and that this is the rate-determining step.[31,32] Finally, recycling in this case is possible, but it is not as good as for the MO reaction – see Fig. S15.†

Electrocatalytic hydrogen oxidative reaction with Pd-grown@Ni/NiO-decorated fibers. The alkaline HOR, which is the bottleneck anode reaction in anion exchange membrane fuel cells, is given by the set of reactions 1:

Tafel Step:

$$2Pd + H_2 \Rightarrow 2PdH_{ads} \quad (1a)$$

Volmer Step:

$$2PdH_{ads} + 2OH^- \Rightarrow 2Pd + 2H_2O + 2e^- \quad (1b)$$

Overall reaction:

$$H_2 + 2OH^- \Rightarrow 2H_2O + 2e^- \quad (1c)$$

H_2 adsorbs on the metallic surface in the Tafel step followed by the Volmer rate-limiting electron release step.[33] While Pt is usually used for that process, Pd can be used as well by adding a second oxophilic metal such as Ni,[34] which improves the Volmer step.[35] Therefore, we selected Pd/Ni system to demonstrate the concept of the metal-entrapment method. Fibers morphology – see Fig. S5† – was selected, following reports on enhanced activity and stability of IrO_x fibers layer coated with IrO_x NPs.[36] Cyclic voltamograms (CVs) of Ni/NiO-decorated fibers and of Pd-grown@Ni/NiO-decorated fibers, shown in Fig. 11(e) and (f), were recorded to display the surface electrical characteristics (Fig. 11(a)). The flat CV features below 0.4 V with Ni/NiO-decorated fibers suggest no hydrogen adsorption/desorption region, which is typical of precious metals. The CV features are the signature of the Pd present in our sample. This observation is similar to our previous results[9] on $PdCeO_2$. The corresponding hydrogen oxidation polarization curves are shown in Fig. 11(b), and the inset shows the mass-normalized activity. Interestingly, Pd-grown@Ni/NiO-decorated fibers displaced strong oxidation current, attributed to hydrogen oxidation. Ni/NiO-decorated fibers' HOR curves show negligible current towards HOR reflecting the role of Pd in Pd-grown@Ni/NiO-decorated fibers. The HOR current at 0.10 V is comparable to those recorded for Pd–W–C,[37] Pd,[38] Pd–CeO_2.[9] Pd-grown@Ni/NiO-decorated fibers were further analyzed to investigate the mass-transport behavior by varying the electrode's rotation speed (Fig. 11(c)). The increase in HOR current with rotation rate confirms that the process is limiting by mass-transport.[39] Pd-grown@Ni/NiO-decorated fibers exhibited reasonable stability for 10 h at 0.37 V *vs.* RHE in H_2-saturated 0.1 M KOH (Fig. 11(d)).

4. Conclusion

Traditionally, 3D dispersion and support of metallic NPs for a variety of applications have been carried out on porous ceramics, glasses, and cross-linked polymers. Here we advance the use of metal for that purpose. Several methods have been developed and are presented, which are based on the entrapment of pre-prepared NPs within the metallic matrices during their reductive formation from the metals' cations; and on the reductive formation of the NPs within pre-prepared metallic matrices, either aggregated porous metals, or metallic foams. Various combinations of metallic NPs and metallic matrices were used, based on Ag, Au, Pt, Pd, Rh, Ir, and Ni. Of the potential applications of dispersed metallic NP, the feasibility of their use in catalysis was demonstrated on the catalyzed reduction of polluting dyes, and on the fuel-cell electrocatalyzed oxidation of hydrogen. We believe that the results shown here can be generalized to other protocols using metal entrapment for any pair of metals, M_1 and M_2, of relevance.

Conflicts of interest

There are no conflicts of interest to declare.

Acknowledgements

This work was partially funded by the Nancy & Stephen Grand Technion Energy Program (GTEP); by the Ministry of Science, Technology & Space of Israel through grant No. 3-12948; by the Israel Science Foundation (ISF) [grant No. 1481/17]; by the Russell Berrie Nanotechnology Institute, Technion.

References

1 J. M. Campelo, D. Luna, R. Luque, J. M. Marinas and A. A. Romero, Sustainable Preparation of Supported Metal Nanoparticles and Their Applications in Catalysis, *ChemSusChem*, 2009, **2**(1), 18–45.
2 Q. L. Zhu and Q. Xu, Immobilization of Ultrafine Metal Nanoparticles to High-Surface-Area Materials and Their Catalytic Applications, *Chem*, 2016, **1**(2), 220–245.
3 J. R. Davis, *Alloying: Understanding the Basics*, ASM International, Materials Park, OH, 2001.

4 Y. Han, H. Xu, Y. Su, Z. Xu, K. Wang and W. Wang, Noble Metal (Pt, Au@Pd) Nanoparticles Supported on Metal Organic Framework (MOF-74) Nanoshuttles as High-Selectivity CO2 Conversion Catalysts, *J. Catal.*, 2019, **370**, 70–78.

5 Z. Zheng, H. Xu, Z. Xu and J. Ge, A Monodispersed Spherical Zr-Based Metal–Organic Framework Catalyst, Pt/Au@Pd@UIO-66, Comprising an Au@Pd Core–Shell Encapsulated in a UIO-66 Center and Its Highly Selective CO2 Hydrogenation to Produce CO, *Small*, 2018, **14**(5), 1–8.

6 Y. Fang, C. Li, J. Bo, J. Henzie, Y. Yamauchi and T. Asahi, Chiral Sensing with Mesoporous Pd@Pt Nanoparticles, *ChemElectroChem*, 2017, **4**(8), 1832–1835.

7 D. Avnir, Recent Progress in the Study of Molecularly Doped Metals, *Adv. Mater.*, 2018, **30**(41), 1–6.

8 D. Avnir, Molecularly Doped Metals, *Acc. Chem. Res.*, 2014, **47**(2), 579–592.

9 N. Ralbag, E. S. Davydova, M. Mann-Lahav, P. Cong, J. He, A. M. Beale, G. S. Grader, D. Avnir and D. R. Dekel, Ceria Entrapped Palladium Novel Composites for Hydrogen Oxidation Reaction in Alkaline Medium, *J. Electrochem. Soc.*, 2020, **167**(5), 054514.

10 N. Ralbag, I. Felner and D. Avnir, Induction of Enhanced Magnetic Behavior in Gold, Silver, and Copper by Doping with SrF E12 O19 Nanoparticles, *Phys. Rev. B*, 2019, **99**(6), 1–7.

11 J. He, B. Ji, S. Koley, U. Banin and D. Avnir, Metallic Conductive Luminescent Film, *ACS Nano*, 2019, **13**(9), 10826–10834.

12 I. Yosef and D. Avnir, Metal-Organic Composites: The Heterogeneous Organic Doping of the Coin Metals-Copper, Silver, and Gold, *Chem. Mater.*, 2006, **18**(25), 5890–5896.

13 K. S. Krishna, C. S. S. Sandeep, R. Philip and M. Eswaramoorthy, Mixing Does the Magic: A Rapid Synthesis of High Surface Area Noble Metal Nanosponges Showing Broadband Nonlinear Optical Response, *ACS Nano*, 2010, **4**(5), 2681–2688.

14 N. Gupta, H. P. Singh and R. K. Sharma, Metal Nanoparticles with High Catalytic Activity in Degradation of Methyl Orange: An Electron Relay Effect, *J. Mol. Catal. A: Chem.*, 2011, **335**(1–2), 248–252.

15 R. Narayanan and M. A. El-sayed, *Shape-Dependent Catalytic Activity of Platinum Nanoparticles in Colloidal Solution*, 2004.

16 J. He, L. Iagher, L. Etgar and D. Avnir, Fine-Tuning of the Metal Work Function by Molecular Doping, *Chem. Commun.*, 2018, **54**(52), 7203–7206.

17 B. Menagen, R. Pedahzur and D. Avnir, Sustained Release from a Metal - Analgesics Entrapped within Biocidal Silver, *Sci. Rep.*, 2017, **7**(1), 1–11.

18 S. Alex and A. Tiwari, Functionalized Gold Nanoparticles: Synthesis, Properties and Applications-A Review, *J. Nanosci. Nanotechnol.*, 2015, **15**(3), 1869–1894.

19 H. Tsunoyama, H. Sakurai, N. Ichikuni, Y. Negishi and T. Tsukuda, Colloidal Gold Nanoparticles as Catalyst for Carbon-Carbon Bond Formation: Application to Aerobic Homocoupling of Phenylboronic Acid in Water, *Langmuir*, 2004, **20**(26), 11293–11296.

20 M. J. Sharif, P. Maity, S. Yamazoe and T. Tsukuda, Selective Hydrogenation of Nitroaromatics by Colloidal Iridium Nanoparticles, *Chem. Lett.*, 2013, **42**(9), 1023–1025.

21 Y. Zhao, J. A. Baeza, N. K. Rao, L. Calvo, M. A. Gilarranz, Y. D. Li and L. Lefferts, Unsupported PVA- and PVP-Stabilized Pd Nanoparticles as Catalyst for Nitrite Hydrogenation in Aqueous Phase, *J. Catal.*, 2014, **318**, 162–169.

22 K. M. Koczkur, S. Mourdikoudis, L. Polavarapu and S. E. Skrabalak, Polyvinylpyrrolidone (PVP) in Nanoparticle Synthesis, *Dalton Trans.*, 2015, **44**(41), 17883–17905.

23 B. Vellaichamy and P. Periakaruppan, Ag Nanoshell Catalyzed Dedying of Industrial Effluents, *RSC Adv.*, 2016, **6**(38), 31653–31660.

24 J. Pakarinen, L. He, A. R. Hassan, Y. Wang, M. Gupta, A. El-Azab and T. R. Allen, Annealing-Induced Lattice Recovery in Room-Temperature Xenon Irradiated CeO2: X-Ray Diffraction and Electron Energy Loss Spectroscopy Experiments, *J. Mater. Res.*, 2015, **30**(9), 1555–1562.

25 M. Bahrami and S. Jafar Hoseini, Simultaneous Formation of Platinum-Based Nanocatalysts and Degradation of Dyes at Oil/Water Interface: Comparative Morphological and Kinetic Studies, *Appl. Organomet. Chem.*, 2018, **32**(1), 1–12.

26 A. K. Ilunga, B. B. Mamba and T. T. I. Nkambule, Fabrication of Palladium and Platinum Nanocatalysts Stabilized by Polyvinylpyrrolidone and Their Use in the Hydrogenolysis of Methyl Orange, *React. Kinet., Mech. Catal.*, 2020, **129**(2), 991–1005.

27 X. Liu, F. Wang, Z. Chen, M. Megharaj and R. Naidu, Heterogeneous Fenton Oxidation of Direct Black G in Dye Effluent Using Functional Kaolin-Supported Nanoscale Zero Iron, *Environ. Sci. Pollut. Res.*, 2014, **21**(3), 1936–1943.

28 K. M. Carroll, A. W. Knoll, H. Wolf and U. Duerig, Explaining the Transition from Diffusion Limited to Reaction Limited Surface Assembly of Molecular Species through Spatial Variations, *Langmuir*, 2018, **34**(1), 73–80.

29 P. Hervés, M. Pérez-Lorenzo, L. M. Liz-Marzán, J. Dzubiella, Y. Lub and M. Ballauff, Catalysis by Metallic Nanoparticles in Aqueous Solution: Model Reactions, *Chem. Soc. Rev.*, 2012, **41**(17), 5577–5587.

30 A. K. Ilunga, B. B. Mamba and T. T. I. Nkambule, Ferricyanide Reduction to Elucidate Kinetic and Electrochemical Activities on the Metal Nanocatalysts Surface, *Chem. Eng. J.*, 2020, **398**(May), 125623.

31 Y. Li, J. Petroski and M. A. El-Sayed, Activation Energy of the Reaction between Hexacyanoferrate(IH) and Thiosulfate Ions Catalyzed by Platinum Nanoparticles, *J. Phys. Chem. B*, 2000, **104**(47), 10956–10959.

32 M. Sakir and M. S. Onses, Solid Substrates Decorated with Ag Nanostructures for the Catalytic Degradation of Methyl Orange, *Results Phys.*, 2019, **12**, 1133–1141.

33 J. Durst, A. Siebel, C. Simon, F. Hasché, J. Herranz and H. A. Gasteiger, New Insights into the Electrochemical Hydrogen Oxidation and Evolution Reaction Mechanism, *Energy Environ. Sci.*, 2014, **7**(7), 2255–2260.

34 M. Alesker, M. Page, M. Shviro, Y. Paska, G. Gershinsky, D. R. Dekel and D. Zitoun, Palladium/Nickel Bifunctional

Electrocatalyst for Hydrogen Oxidation Reaction in Alkaline Membrane Fuel Cell, *J. Power Sources*, 2016, **304**, 332–339.

35 D. Strmcnik, M. Uchimura, C. Wang, R. Subbaraman, N. Danilovic, D. van der Vliet, A. P. Paulikas, V. R. Stamenkovic and N. M. Markovic, Improving the Hydrogen Oxidation Reaction Rate by Promotion of Hydroxyl Adsorption, *Nat. Chem.*, 2013, **5**(4), 300–306.

36 F. Hegge, F. Lombeck, E. Cruz Ortiz, L. Bohn, M. von Holst, M. Kroschel, J. Hübner, M. Breitwieser, P. Strasser and S. Vierrath, Efficient and Stable Low Iridium Loaded Anodes for PEM Water Electrolysis Made Possible by Nanofiber Interlayers, *ACS Appl. Energy Mater.*, 2020, **3**(9), 8276–8284.

37 A. C. Arulrajan, P. Subramanian, R. K. Singh and A. Schechter, Pd-Decorated Tungsten as Pt-Free Bimetallic Catalysts for Hydrogen Oxidation Reaction in Alkaline Electrolyte, *Isr. J. Chem.*, 2020, **60**(5–6), 563–569.

38 V. Yarmiayev, M. Alesker, A. Muzikansky, M. Zysler and D. Zitoun, Enhancement of Palladium HOR Activity in Alkaline Conditions through Ceria Surface Doping, *J. Electrochem. Soc.*, 2019, **166**(7), F3234–F3239.

39 E. R. Hamo, R. K. Singh, J. C. Douglin, S. Chen, M. B. Hassine, E. Carbo-Argibay, S. Lu, H. Wang, P. J. Ferreira, B. A. Rosen, *et al.*, Carbide-Supported PtRu Catalysts for Hydrogen Oxidation Reaction in Alkaline Electrolyte, *ACS Catal.*, 2021, **11**(2), 932–947.

40 A. Landman, S. Hadash, G. E. Shter, A. Ben-Azaria, H. Dotan, A. Rothschild and G. S. Grader, High Performance Core/Shell Ni/Ni$(OH)_2$ Electrospun Nanofiber Anodes for Decoupled Water Splitting, *Adv. Funct. Mater.*, 2021, **31**, 2008118.